Topological Surface Acoustic Waves

Zi-Dong Zhang,[1] Si-Yuan Yu,[1,2,*] Hao Ge,[1] Ji-Qian Wang,[1] Hong-Fei Wang,[1] Kang-Fu Liu,[3] Tao Wu,[3] Cheng He,[1,2] Ming-Hui Lu,[1,2,†] and Yan-Feng Chen[1,2,‡]

[1] *National Laboratory of Solid State Microstructures and Department of Materials Science and Engineering, Nanjing University, Nanjing 210093, China*

[2] *Jiangsu Key Laboratory of Artificial Functional Materials, Nanjing University, Nanjing 210093, China*

[3] *School of Information Science and Technology, Shanghai Tech University, Shanghai 201210, China*

(Received 7 February 2021; revised 12 September 2021; accepted 16 September 2021; published 7 October 2021)

Topological materials for classical waves, e.g., electromagnetic and acoustic waves, have attracted growing interest, mainly due to the robustness, low loss, and new artificial degree of freedom conferred by their boundaries. Surface acoustic waves (SAWs), as widely used information carriers of microdevice relevance, are ubiquitous in today's wireless communication and sensing networks. Herein, we report the implementation of a SAW topological insulator based on a monolithically integrated platform. By using a miniature acoustic resonator array working tens of megahertz on a piezoelectric half-space, we successfully endow electrically pumped Rayleigh-type SAWs with the "spin-momentum locking" feature, enabling solid-state acoustic waves on the "one-dimensional interface of the two-dimensional surface on the three-dimensional volume" detour arbitrarily and pass through defects and intersections with much smaller losses than those incurred with any other solutions. These revolutionary topological SAWs may open an avenue for monolithic electronic-(photonic)-phononic circuits with ultrahigh performance and advanced functionalities in, e.g., future mobile communicating, sensing, and quantum-information processing.

DOI: 10.1103/PhysRevApplied.16.044008

I. INTRODUCTION

Surface-acoustic-wave (SAW) technology is the most representative phonon technology to date. These miniature "earthquakes on chips" can be found in versatile scenarios, including wireless communications, sensors, consumer electronics, diagnostics, industrial monitoring systems, satellites, and deep-space exploration units [1]. Similar to light propagation in transparent media, SAW transmission in rigid materials exhibits extremely low loss. Advantageously, because phonons have much slower propagation speeds than photons (by a factor of $1/10^5$), the device and equipment footprints are much smaller when SAWs are used to load, process, and modulate signals in any band. Particularly, when working at frequencies between tens of MHz and several GHz, planar SAWs have appropriate wavelengths to participate in optomechanical interactions in integrated optics [2–4], manipulate particles in fluids [5,6], and detect and control elementary excitations in solids in both the classical and quantum-mechanical regimes [7–9].

In recent years, various topological states in electronic systems have been topics of intensive investigation in condensed-matter physics [10–12]. Since the existence of topological properties depends largely on the band structure itself, the topological states and features found in electronic systems can also be implemented in bosonic systems, leading to the emergence of topological photonics [13–22], mechanics [23–27], and acoustics [28–44]. An underlying motivation behind these explorations is that they offer an unparalleled transport mechanism with backscattering suppression, leading to a revolutionary reduction in transmission losses, arbitrarily designed transmission paths, and defect robustness in device processing, regardless of the system. However, although the field of topological acoustics has yielded some groundbreaking work in both fluids [37] and solids [38–41], even in miniaturized systems [42–44], a topological state for SAWs has not yet been verified.

In this paper, we report the realization of a SAW (in particular, Rayleigh wave) topological insulator (TI), as well as an experimental demonstration of an analog of the quantum spin Hall effect (QSHE) at the TI boundaries, implemented monolithically on an interdigital transducer (IDT)-based platform operating at frequencies of tens of megahertz. The Rayleigh-SAW transmission on

*yusiyuan@nju.edu.cn
†luminghui@nju.edu.cn
‡yfchen@nju.edu.cn

these designable TI boundaries exhibits the so-called "spin-momentum locking" property, which fundamentally suppresses unwanted but crucial backscattering. Regardless of the presence of sharp bends in high degrees of freedom or structural defects encountered, it has been confirmed that the transmittance is not significantly reduced, thus demonstrating the TI boundaries can serve as revolutionary ideal SAW waveguides with low loss and high flexibility. In fact, our miniaturized microwave-acoustic experiment itself provides a practical chip-scale topological prototype for SAWs, which monolithically integrates SAW TI materials, electrical pumping source, and receivers together, opening a promising route for future high-performance electronic-(photonic)-phononic integrates circuits (in terms of energy efficiency, information capacity, and signal integrity) with various functionalities.

II. RESULTS AND DISCUSSION

A. Design of a surface acoustic topological insulator on a piezoelectric $LiNbO_3$ substrate

We investigate the SAW topological phenomenon by preparing artificial periodical microstructures on a half-space. These microstructures are called SAW phononic crystals (PnCs) [45–54]. Specifically, in this research, this microstructure is composed of miniaturized acoustic resonators (i.e., micropillars) arranged in a honeycomb lattice, as illustrated in Fig. 1(a). This quasi-two-dimensional (2D) artificial material is referred to as surface phononic graphene [53], because the SAWs on its surface have a band structure similar to that of electrons in graphene, with Dirac points at the Brillouin zone (BZ) corners [54]. To facilitate SAWs' electrical pumping and transduction, the half-space substrate is usually piezoelectric, e.g., lithium niobate ($LiNbO_3$) [48,49]. Note that these Dirac points are protected by the symmetry of the honeycomb lattice but not accidental degeneracy. Therefore, it is easy to obtain, regardless of the materials used for the substrate and the resonators.

Based on the SAW Dirac points at the BZ corners, we adopt a highly effective method, namely, zone folding [15,18], to achieve quadruple degeneracy (i.e., double Dirac cones) to simulate electronic spins in this acoustic system. Specifically, we slightly adjust the original honeycomb lattice, in which a composite hexagonal unit cell containing six micropillars is created, as shown in

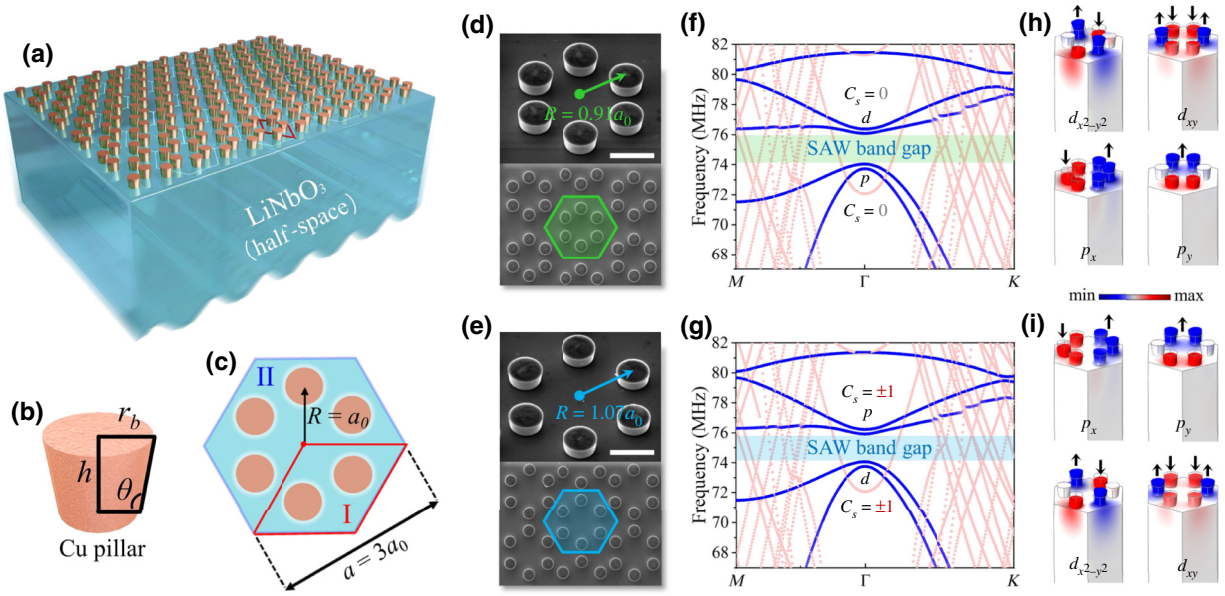

FIG. 1. (a) Schematics of the PnC for SAWs used in this study, i.e., a honeycomb lattice composed of identical miniaturized resonator pillars on a $LiNbO_3$ half-space. (b) Enlarged view of each micropillar made of copper (Cu) with an inverted truncated conical shape due to our fabrication process. (c) Top view of the unit cells of the SAW-PnC: (I) original diamond cell with two micropillars and (II) threefold-larger hexagonal cell with six micropillars for the zone-folding implementation. Originally, the honeycomb lattice has a pillar-center distance $R = a_0$. (d), (e) SEM images of two elaborately fabricated SAW PnCs, one with a shrunken lattice ($R = 0.91a_0$) and another with an expanded lattice ($R = 1.07\ a_0$), respectively. Insets are tilted views of the two samples, where the scale bars represent 10 μm. (f), (g) Calculated band structures of the two PnCs. The blue lines and dots represent Rayleigh-type SAW modes. The pink lines and dots represent ineffectual bulk acoustic wave modes brought by the calculation; see Notes S2 and S3 within the Supplemental Material. The two PnCs are SAW insulators with an overlapping band gap from approximately 72 to 74 MHz. Essentially, there is a band inversion for their p_x/p_y and d_{xy}/d_{x2-y2} modes (like p/d orbitals of electrons), corresponding to a topological transition from an SAW ordinary insulator [OI, zero spin Chern number (C_s)] to a SAW topological insulator (TI, none-zero C_s). (h), (i) Simulated field profiles of the vertical displacement at the top surface of the six micropillar unit cells for the p/d eigenmodes, corresponding to the Rayleigh-type SAW OI and TI, respectively. The black arrows indicate the directions of the surface mechanical vibrations.

Fig. 1(c), to implement zone folding while leaving the system symmetry unchanged. This operation provides us with a Rayleigh-type SAW Dirac semimetal with artificial spin analogs. Next, we can use it to form two SAW insulators with different topological properties. Formally, we modify the distance of each micropillar from the center of the hexagonal cell, depicted as R in the figure, to form different kinds of SAW PnCs. Initially ($R = a_0$), SAW PnC is a standard honeycomb lattice with Dirac points. When R increases or decreases, the SAW Dirac points will disappear, and the PnC will thus transition from a SAW semimetal to a SAW insulator. Experimentally, we prepare two types of SAW PnCs, as shown in the SEM images presented in Figs. 1(d) and 1(e), with R equal to $0.91a_0$ and $1.07a_0$, respectively. The lattice periods of the two SAW PnCs are the same ($3a_0$, 42 μm). Moreover, all the micropillars are geometrically identical, with r_b, h, and θ equal to 4.3 μm, 7.2 μm, and 84°, respectively, as shown in Fig. 1(b). Our samples are prepared using a LIGA-like process [54]. Calculated band structures of these two SAW PnCs are shown in Figs. 1(f) and 1(g). According to the acoustic energy distribution of each eigenmode, all SAW modes can be distinguished [54,55]. Due to the breaking of parity symmetry [15], in the vicinity of the original Dirac frequency, a SAW band gap of approximately 2 MHz (2.7%) appears in both, with a frequency overlap from approximately 74 to 76 MHz. The original double Dirac cone forms two pairs of dispersions located at the top and bottom of the SAW band gap.

Specifically, for the case of $R = 0.91a_0$ ($R < a_0$), both modes at the high frequencies of the band gap have quadrupolelike vibrational properties, such as the d_{x2-y2} and d_{xy} orbitals of electrons, whereas both modes at the low frequencies are dipolelike, such as the p_x and p_y orbitals of electrons, as shown by the vertical displacement fields depicted in Fig. 1(h). For $R = 1.07$ a_0 ($R > a_0$), the situation is reversed, with p_x and p_y at high frequencies and d_{x2-y2} and d_{xy} at low frequencies, as shown in Fig. 1(i). From the characteristics of this standard band inversion, it can be inferred that the two SAW-PnC bands have different topological properties. According to theoretical analyses, the band of the SAW PnC with $R < a_0$ has zero spin Chern numbers (i.e., is topologically trivial); therefore, this PnC can be called a SAW ordinary insulator (OI). In contrast, the band of the SAW PnC with $R > a_0$ has nonzero (± 1) spin Chern numbers (i.e., is topologically nontrivial); therefore, this PnC can be called a SAW TI. Consequently, artificial spin $\pm$½ properties for the bulk states can be achieved through linear combinations of these symmetric p/d modes [15]. Note that all the SAW modes mentioned above are true Rayleigh-type modes (see Appendices A and B).

B. Experimental demonstration of helical edge states for SAWs

To further construct useful SAW edge state(s), three different TI-OI interfaces, i.e., a zigzag interface, an armchair interface, and a straight (deformed armchair) interface, are investigated. For the abovementioned TI-OI interfaces, although they all have SAW edge states with comparable properties, in some cases, an obvious minigap will appear within the edge state frequencies due to the relatively large symmetry mismatch between the micropillar lattice and the anisotropic piezoelectric substrate [56] (see Appendix C). For example, this minigap is obvious for the zigzag TI-OI interface, with a relative bandwidth greater than 1%. Fortunately, the minigaps for the armchair and straight TI-OI interfaces are imperceptible, with relative bandwidths less than 0.012%, i.e., so small that we cannot even detect or use them in practice. For conciseness and ease of demonstration of the SAW TI-OI boundary, i.e., the topologically protected SAW transmission channel, we therefore choose the straight TI-OI interface and fabricated the sample depicted in the SEM image shown in Fig. 2(a). Figure 2(b) shows the projected SAW band diagram of this interface (both numerically calculated and experimentally measured). An obvious pair of SAW helical edge states appear gapless between the overlapped OI-TI band gap.

Experimental results obtained with a laser Doppler vibrometer fully confirm the existence of the TI-OI helical edge states. In the experiment, planar SAWs of different frequencies are incident on the TI-OI interface. When the frequency is in the passband of the TI-OI, e.g., at 72 MHz in Figs. 2(c) and 2(d), no edge modes but only bulk SAW modes will be observed around the interface. When the frequency is in the overlapping insulating band of the TI-OI, e.g., at 75 MHz in Figs. 2(e) and 2(f), the SAWs are highly located and propagate along with the TI-OI interface. The measured and calculated results are consistent, as shown in Video SI within the Supplemental Material [54]. These two edge states are hybrids of a symmetric vibrational mode $S = (p_x + d_{x2-y2})/\sqrt{2}$ and an antisymmetric vibrational mode $A = (p_y + d_{xy})/\sqrt{2}$, formed as $S + iA$ and $S - iA$, respectively. The S and A bases are protected by pseudo-time-reversal symmetry ($T_p^2 = -1$), as "$+S \xrightarrow{T_p} +A \xrightarrow{T_p} -S \xrightarrow{T_p} \cdots$" [15,31,39]. The measured time-domain SAW displacement fields of the two edge states, shown in Figs. 2(g) and 2(h), clearly exhibit clockwise ($S + iA$) and counterclockwise ($S - iA$) features. A SAW edge mode running forward shows a characteristic spatiotemporal pattern: "$+S \rightarrow +A \rightarrow -S \rightarrow \cdots$." In contrast, the reverse edge mode also has a distinctive but different way: "$+S \rightarrow -A \rightarrow -S \rightarrow \cdots$." All these dynamic visual results are conclusive evidence of SAW artificial spin $\pm$½ states locked with momentum, i.e., spin +½ only in the forward direction and spin −½ only in the

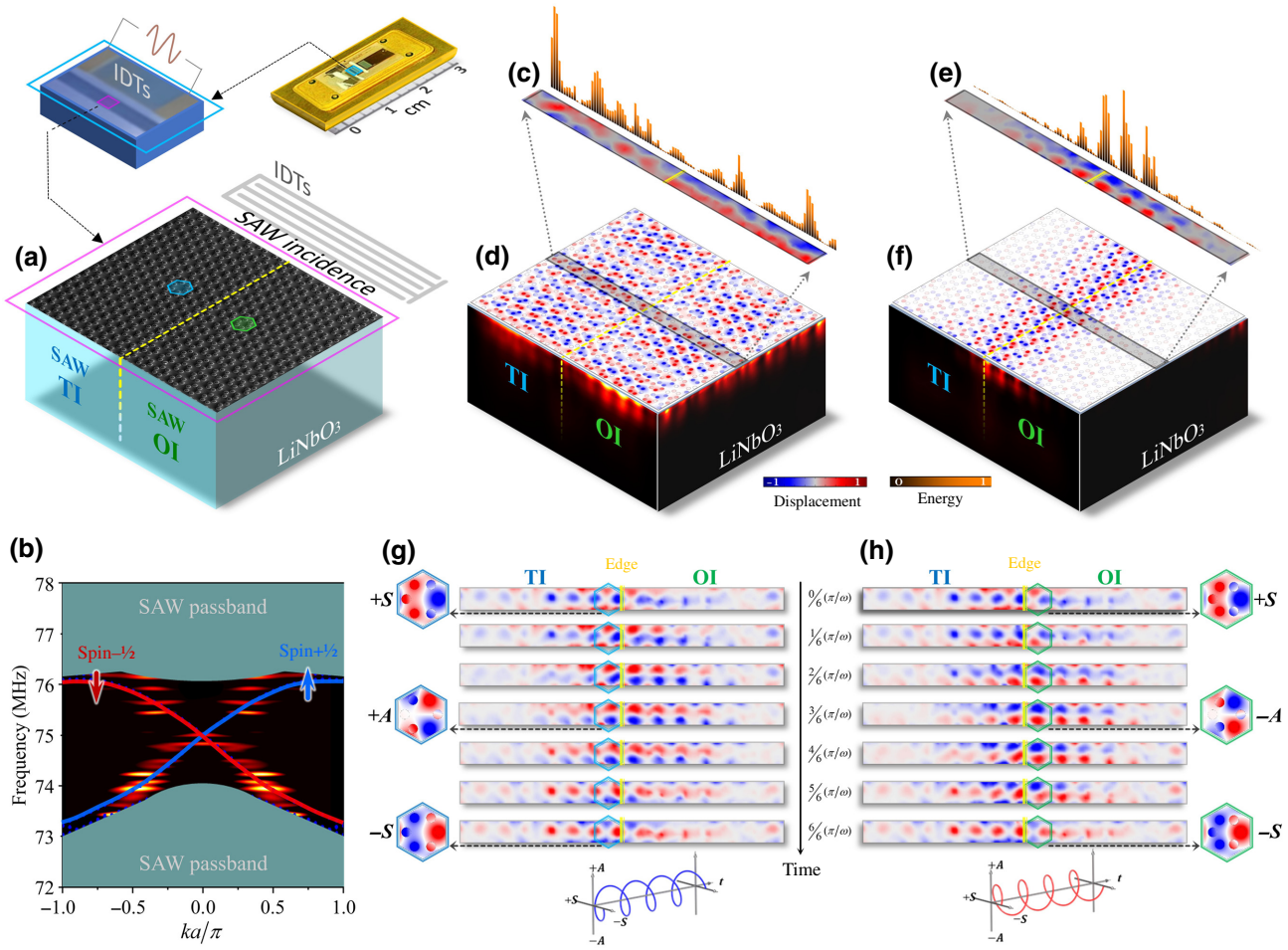

FIG. 2. (a) Adjacent SAW TI-OI sample used in our experiments. On the surface of a *yz*-cut $LiNbO_3$ substrate, planar SAWs of different frequencies are evoked by broadband IDTs and incident on a straight TI-OI interface (yellow dashed line). (b) Experimentally measured (heat map) and numerically simulated (solid lines) projected band diagrams of the interface, showing two gapless helical edge states of SAWs. (c), (d) Measured and simulated out-of-plane displacement fields and energy distributions in the vicinity of the TI-OI interface at 72 MHz, respectively. No TI-OI edge mode, but conducting SAWs are observed inside the TI and OI everywhere. (e), (f) Similar displacement fields and energy distributions at 75 MHz, i.e., in the TI-OI band gap, respectively. SAWs are observed only localized and propagating along with the TI-OI interface. (g), (h) Experimentally recorded temporal evolution of the out-of-plane displacement fields when the SAWs are selectively excited forward and backward along with the TI-OI interface, respectively, confirming the SAW pseudospins ±½ represented in the *S*/*A* basis: time-dependent anticlockwise SAW spin+½ ($S+iA$) and clockwise SAW spin−½ ($S-iA$), respectively.

backward order, which intuitively characterizes an SAW analogous QSHE.

C. Basic elements in topological SAW-integrated circuits.

According to current knowledge, bosonic spin flipping from ±½ cannot be achieved in a static, i.e., no external field, no (wavelength-comparable) standing-wave resonance environment (i.e., no effective "magnetic" impurities). Hence, due to the spin-momentum-locked SAWs offered by the TI-OI interface, SAW backscattering [the conversion between forward ($+k$) and backward ($-k$) transport SAW modes] can be intrinsically suppressed, making SAW waveguiding along with the TI-OI interface robust against various defects, e.g., fabrication imperfections. It is worth noting that it also provides a SAW waveguide solution that can be bent arbitrarily. Experimentally, both a vacancy defect and a sharp detour are testably placed on the SAW TI-OI interface to demonstrate its ideal 2D SAW waveguiding capability. The left panels of Figs. 3(a) and 3(b) show the experimental scheme. Both simulated and measured SAW energy distributions are shown in the right panels of the figures, confirming both the robustness and flexibility of the SAW waveguiding. The SAWs detour around the defect and sharp bends while preserving almost all transmission energy. As a comparison, for previous SAW waveguides designed using

line defects in SAW PnC (in principle, an OI-OI interface), similar configurations severely inhibit SAW forward propagation due to strong backscattering [54]. Moreover, splitting and converging, as basic functions in integrated circuitry, could also be achieved by the TI-OI interface. A simple experimental demonstration is shown in Fig. 3(c). When an incident SAW excited by the IDTs on the right enters a beam splitter made from TI-OI interfaces, it is successfully split into two beams without causing reflection. Due to reciprocity, its time-reversal process, i.e., SAW convergence, is natural. Additionally, high-quality 2D SAW resonators accompanied by waveguides by introducing an SAW whispering gallery made of a SAW TI-OI closed loop is practically available, providing future on-chip 2D-versatile SAW filters, multiplexers, modulators, switches, etc., all with topological protection.

D. SAW transmission line with TI-OI interfaces embedded

We also conduct a comparative experiment of SAW transmission lines, as shown in the diagram presented in Fig. 4(a). Two broadband IDTs, one acting as a SAW emitter and the other as a SAW receiver, are placed face to face on the surface of a *yz*-cut $LiNbO_3$ substrate. Between the two IDTs, we prepare a PnC ribbon consisting of TI and OI sandwiches, forming ten straight TI-OI interfaces (not all of which are shown in the diagram) along the direction of SAW emission. Figure 4(b) shows a false-color SEM image of one of the straight SAW TI-OI interfaces in our sample. For comparison, we also prepare samples with only an OI region or only a TI region between the two IDTs. The overall size of each sample is exactly the same.

Measurement results for the SAW transmission spectra from 70–80 MHz are shown in Fig. 4(d). For the cases with only the TI or only the OI between the two IDTs, their transmittance spectra are similar, and the transmittance drops significantly after 73 MHz. In the first band gap (73.72–76.08 MHz for the OI case; 73.75–75.92 MHz for the TI case), the reduction reaches approximately 30 dB, indicating excellent SAW insulation. In the higher-frequency second band gap (over 76.84 MHz for the OI case; over 76.74 MHz for the TI case), the SAW transmittance is also extremely low. For the sample with ten straight TI-OI interfaces, the transmittance situation is significantly different. In the TI-OI band gap, since the interface has begun to participate in SAW transmission, the total transmittance is improved by nearly 20 dB, thus fully proving the existence of the SAW edge states (considering that the samples are not otherwise different). To fully validate our experimental results, we also perform numerical simulations. The calculated transmittance is consistent with the experimental results, as shown in Fig. 4(e). Some differences in the in-band suppression values are due to

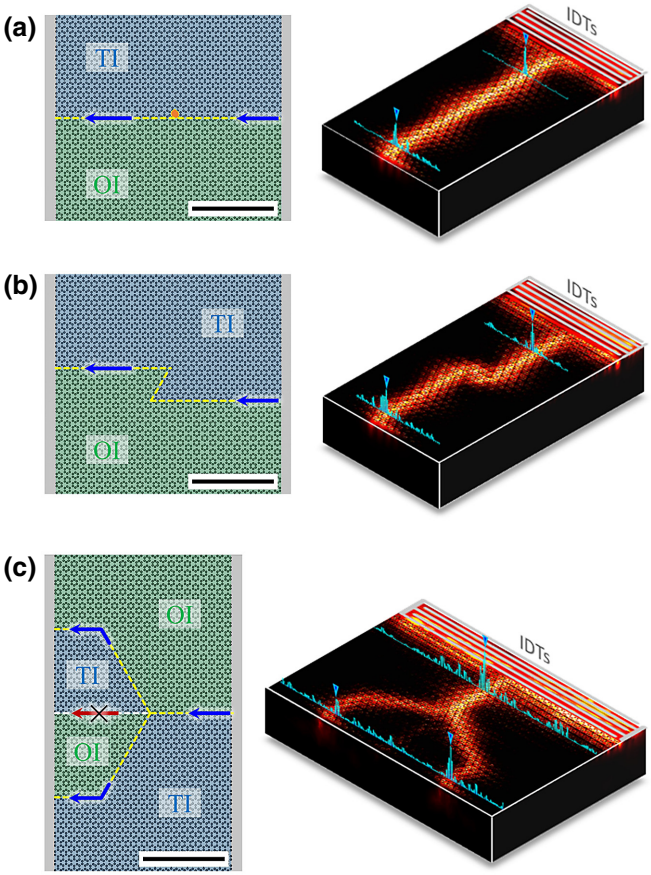

FIG. 3. Left: schematics of different SAW TI-OI interfaces to demonstrate (a) defect robustness. The orange dot indicates a random vacancy defect, (b) geometrical flexibility, and (c) splitting capability. The green and blue regions correspond to SAW OI and TI, respectively, the yellow dotted lines indicate the TI-OI interfaces, and the scale bars represent 400 μm. Right: heat maps are calculated elastic energy-density distributions for SAWs working at frequency within the bulk TI-OI band gap (74.5 MHz); cyan bars are experimental results measured along two straight lines cut through the TI-OI interfaces in front of and behind the defect (a), bends (b), and splitter (c).

the different distances from the IDTs to the PnCs between our simulation model and the experimental sample. Additionally, the simulated spectra indicate the bulk modes' excitation between the first and second TI-OI band gaps. The main feature of topological edge states is their robustness against imperfections and sharp bends. To verify this property, we fabricate a sample consisting of "Z"-shaped TI-OI interfaces, each with two 120° bends, as shown in the false-color SEM image presented in Fig. 4(c). According to the results of both experiments [Fig. 4(d)], the SAW transmission performance of the "Z"-shaped sample is similar to that of the straight-interface sample. In the TI-OI band gap, the SAW transmittance of the "Z"-shaped sample is close to 20 dB higher than that of the TI and OI samples, which indirectly demonstrates that the SAWs

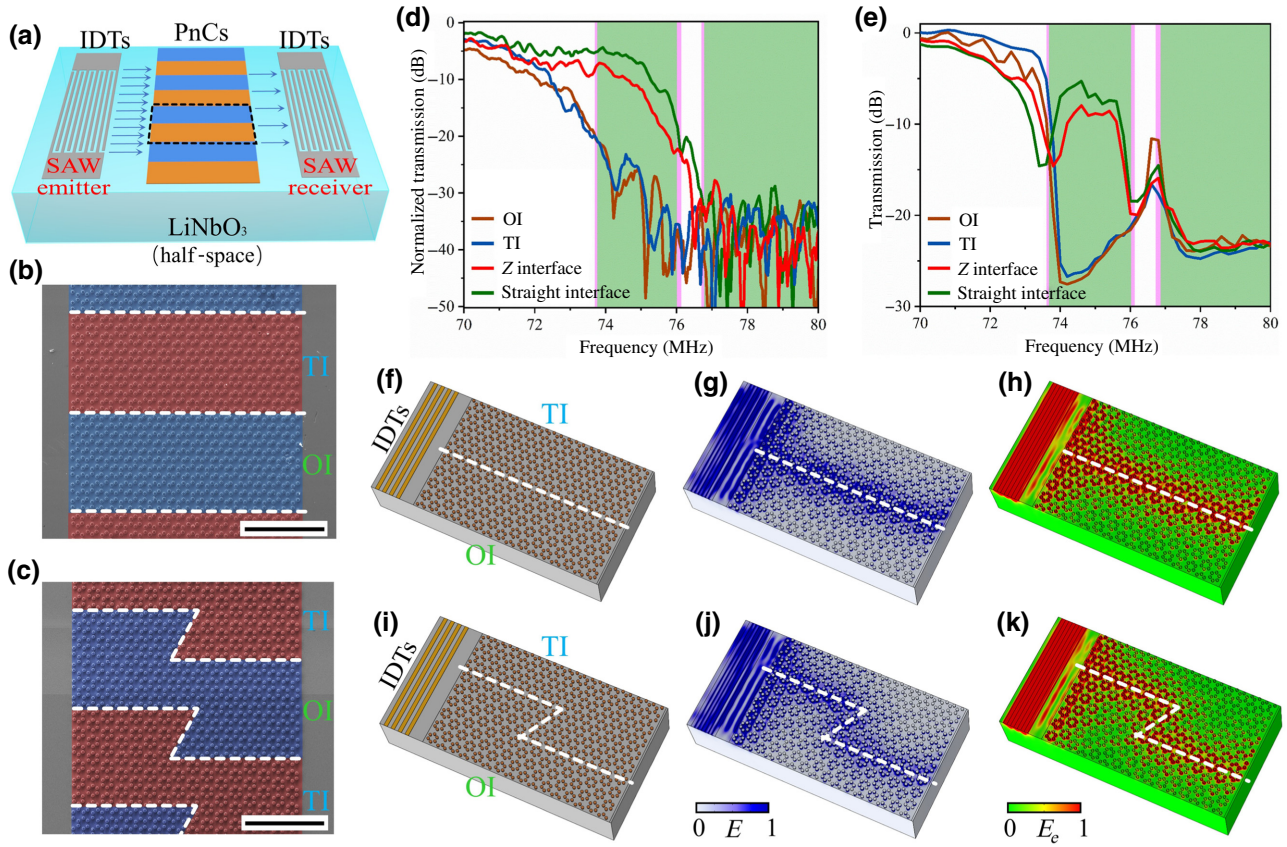

FIG. 4. (a) Schematic of our experiments in a SAW transmission line. IDTs are used to excite and receive SAWs. The black frame surrounds a periodic SAW-PnC structure. (b), (c) Top-view SEM images of the fabricated samples, including straight and "Z"-shaped topological interfaces, where the scale bars represent 200 μm. The red and blue regions correspond to SAW-OI and SAW-TI, respectively. (d), (e) Measured and simulated transmission spectra for the straight and "Z"-shaped TI-OI interfaces, respectively. The red- and green-shaded regions represent the band gaps of the OI and TI, respectively. (f)–(h), (i)–(k) Elastic stored energy densities and electric energy densities for the two distinctly shaped TI-OI interfaces at 75 MHz.

make a detour around the 120° bends with the considerable transmission.

The reason we use multiple TI-OI interfaces in our PnC ribbon is because of the following reasons: we need broadband IDTs for experiments. The existing broadband IDTs cannot have a small aperture (for surface-acoustic-wave emission), so the aperture of our IDTs is much larger than the effective width of a single SAW waveguide (their specific size is about hundreds of micrometers compared to tens of micrometers). Under such an experimental framework, we can hardly measure the difference in S_{21} parameters due to a single SAW waveguide.

III. CONCLUSION

We experimentally demonstrate topological protected SAWs (particularly the Rayleigh-type SAWs) on a piezoelectric $LiNbO_3$ half-space. Employing the zone-folding method and breaking the parity symmetry of a Rayleigh-type SAW Dirac semimetal, two kinds of SAW insulators with overlapping band gaps and different topological properties are formed. A revolutionary SAW transport mechanism is thus manifested at the boundaries of the two insulators, with artificial pseudospin $\pm$½ states for SAWs locked with momentum. It offers a near-perfect "1D surface of a 2D surface on a 3D volume" phononic channel with extremely low loss and high flexibility. This may pave the way for the next-generation high-performance phonon-based information processing (in terms of energy efficiency, information capacity, and signal integrity) on various commonly used piezoelectric materials (e.g., $LiNbO_3$, AlN, and GaN) or many emerging 2D piezoelectric materials. Due to its structural simplicity and (electromechanical) transducing accessibility, the present prototype in this work is thoroughly scalable to operate from several MHz to tens of GHz. Moreover, by further optimizing in its material selection, geometrical configuration [54], and even through topology optimization [57], its working bandwidth is expected to exceed 10% or even higher.

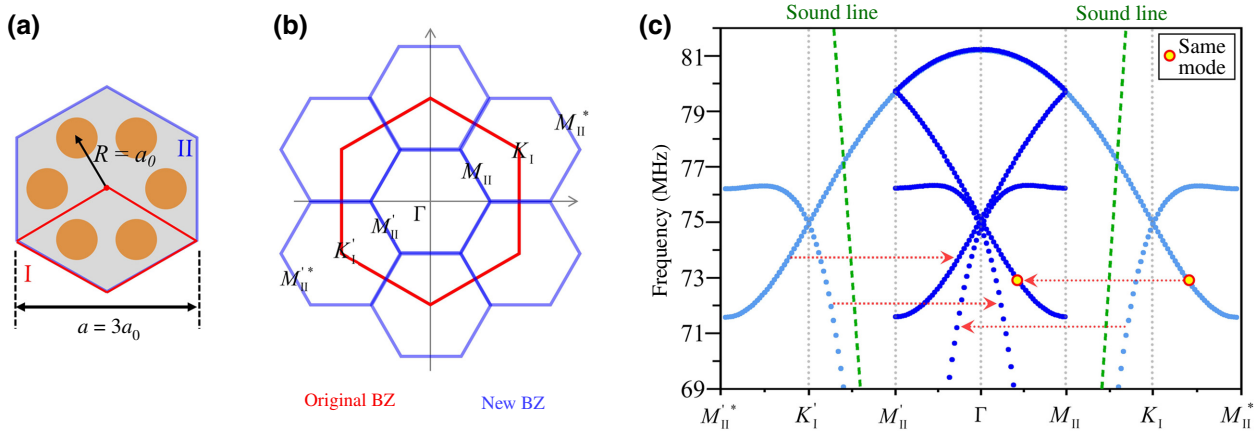

FIG. 5. (a) Two choices of unit cells of the same phononic crystal in the honeycomb lattice. Cell I contains two pillars, triple-sized cell II has six pillars. (b) Two types of BZs according to cell I and cell 2, respectively. (c) SAW dispersions in the extended BZs, along the direction from M_{II}'*, K_I', M_{II}', Γ, M_{II}, K_I to M_{II}^*. Red dotted arrows indicate the nonphysical band folding, i.e., $\mathbf{G} + \mathbf{k}_0 \rightarrow \mathbf{k}_0$, from extended Brillouin zones to the reduced (first) Brillouin zone. The red circle indicates the same mode. This mode "appears" in the reduced (first) Brillouin zone and inside the (green dotted) sound cone, but it locates at the higher Brillouin zones far away from the Γ point. From the perspective of the extended Brillouin zone, the real position of this mode is below the sound line. The fourfold degeneracy appears at the Γ point of the reduced (first) Brillouin zone is folded from two twofold degeneracies at the K_I and K_I' points of the extended Brillouin zones, which are physically below the sound line.

ACKNOWLEDGMENTS

The work is jointly supported by the National Key R&D Program of China (Grants No. 2017YFA0305100 and No. 2017YFA0303702) and the National Natural Science Foundation of China (Grants No. 11890702, No. 51702152, No. 51721001, and No. 51732006). We also acknowledge the support of the Natural Science Foundation of Jiangsu Province, Fundamental Research

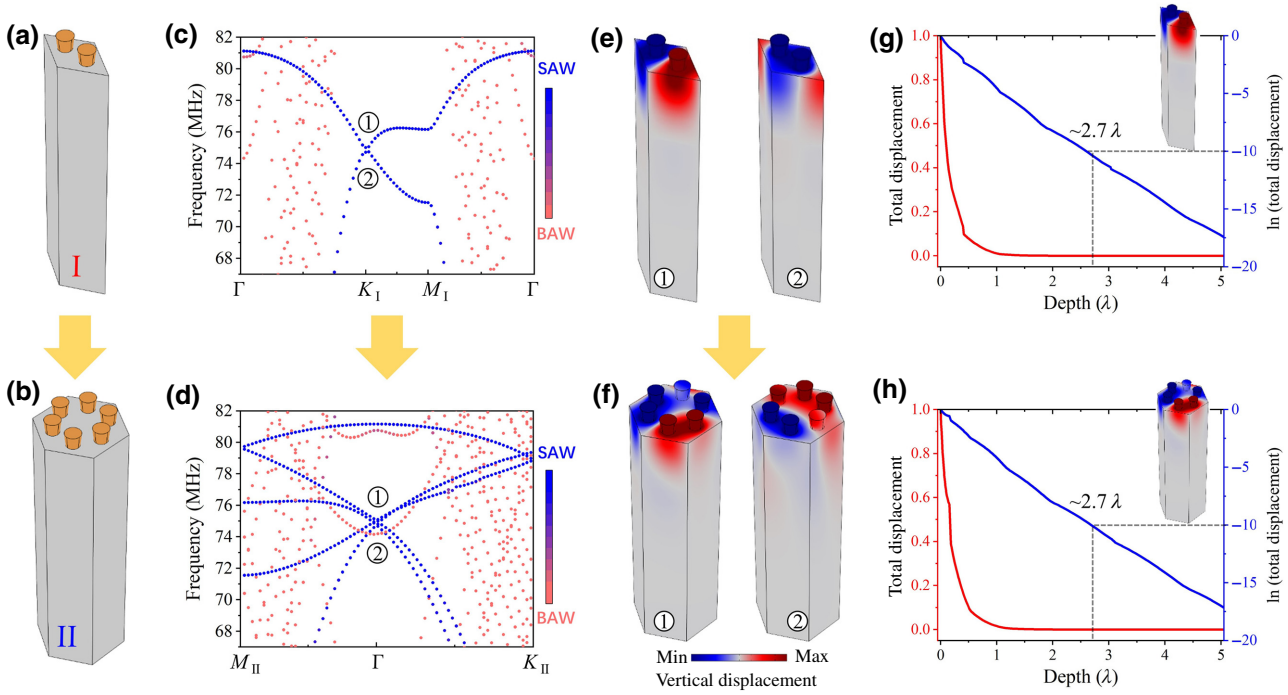

FIG. 6. (a), (b) 3D model of unit cell I and II. (c), (d) Calculated band structures for the two cases. SAW degeneracy appears at the K_I (also K_I') point in (c), and appears at the Γ point in (d). (e), (f) Vertical displacement fields of two degenerate modes (âŚă and âŚą) shown in (c) and (d), respectively. (g), (h) Total displacement as a function of depth of mode âŚă shown in (c) and (d), respectively, by using the same analysis of reference [55]. It confirmed that all these modes are true Rayleigh-type surface acoustic waves (RSAWs).

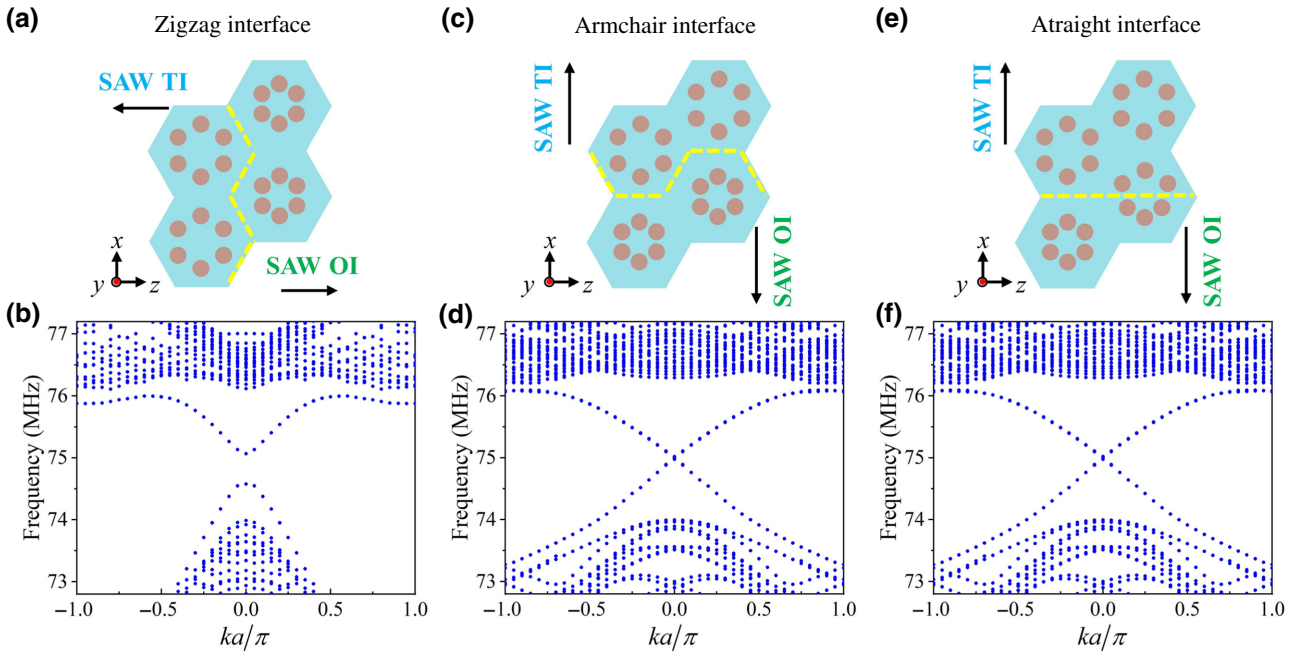

FIG. 7. Projected SAW band structures for different TI-OI interfaces. (a), (c), (e) Schematic zigzag, armchair, and deformed armchair interfaces, respectively, between SAW OI and SAW TI. (b), (d), (f), SAW band structures of the three TI-OI interfaces.

Funds for Central Universities, and the Academic Program Development of Jiangsu Higher Education (PAPD).

APPENDIX A: THE ORIGIN OF THE SAW FOURFOLD DEGENERACY AT THE Γ POINT

Figures 5(a) and 5(b) are two choices of unit cells of the same phononic crystal in the honeycomb lattice and their corresponding two types of Brillouin zones. Figure 5(c) shows that the fourfold degeneracy appears at the Γ point of the reduced (first) Brillouin zone is folded from two twofold degeneracies at the K_{I} and K_{I}' points of the extended Brillouin zones [58,59], and it is physically below the sound line.

APPENDIX B: ANALYSIS FOR RAYLEIGH-TYPE SURFACE-ACOUSTIC-WAVE MODES

We analyze all these degeneracy modes by adopting a method reported in Refs. [55,60]. As the results shown in Fig. 6, these degeneracy modes, whether they are at the Γ point or at the $K_{\mathrm{I}}/K_{\mathrm{I}}'$ points, are the same. They are confirmed true RSAW modes by their appearance, energy distribution criterion, and penetration depth. We also provide a sketch of all these modes [54]; see Video SII within the Supplemental Material.

APPENDIX C: INFLUENCE OF DIFFERENT TI-OI INTERFACES

Three different TI-OI interfaces, i.e., a zigzag interface, an armchair interface, and a straight (deformed armchair) interface, as shown in Fig. 7, are investigated. An obvious minigap will appear within the edge state frequencies for the zigzag interface due to the relatively large symmetry mismatch between the micropillar lattice and the anisotropic piezoelectric substrate. Fortunately, the minigaps for the armchair and straight TI-OI interfaces are imperceptible.

[1] P. Delsing, *et al.*, The 2019 surface acoustic waves roadmap, J. Phys. D. Appl. Phys. **52**, 353001 (2019).
[2] K. C. Balram, M. I. Davanço, J. D. Song, and K. Srinivasan, Coherent coupling between radiofrequency, optical and acoustic waves in piezo-optomechanical circuits, Nat. Photonics **10**, 346 (2016).
[3] M. Forsch, R. Stockill, A. Wallucks, I. Marinković, C. Gärtner, R. A. Norte, F. van Otten, A. Fiore, K. Srinivasan, and S. Gröblacher, Microwave-to-optics conversion using a mechanical oscillator in its quantum ground state, Nat. Phys. **16**, 69 (2020).
[4] A. H. Safavi-Naeini, D. V. A. N. Thourhout, R. Baets, and R. van Laer, Controlling phonons and photons at the wavelength scale: Integrated photonics meets integrated phononics, Optica **6**, 2334 (2019).
[5] Z. Tian, S. Yang, P. H. Huang, Z. Wang, P. Zhang, Y. Gu, H. Bachman, C. Chen, M. Wu, Y. Xie, and T. J. Huang, Wave

number–spiral acoustic tweezers for dynamic and reconfigurable manipulation of particles and cells, Sci. Adv. **5**, eaau6062 (2019).

[6] A. Ozcelik, J. Rufo, F. Guo, Y. Gu, P. Li, J. Lata, and T. J. Huang, Acoustic tweezers for the life sciences, Nat. Methods. **15**, 1021 (2018).

[7] S. J. Whiteley, G. Wolfowicz, C. P. Anderson, A. Bourassa, H. Ma, M. Ye, G. Koolstra, K. J. Satzinger, M. V. Holt, F. J. Heremans, A. N. Cleland, D. I. Schuster, G. Galli, and D. D. Awschalom, Spin–phonon interactions in silicon carbide addressed by Gaussian acoustics, Nat. Phys. **15**, 490 (2019).

[8] A. Bienfait, K. J. Satzinger, Y. P. Zhong, H. S. Chang, M. H. Chou, C. R. Conner, É Dumur, J. Grebel, G. A. Peairs, R. G. Povey, and A. N. Cleland, Phonon-mediated quantum state transfer and remote qubit entanglement, Science **364**, 368 (2019).

[9] K. J. Satzinger, Y. P. Zhong, H. S. Chang, G. A. Peairs, A. Bienfait, M. H. Chou, A. Y. Cleland, C. R. Conner, É Dumur, J. Grebel, I. Gutierrez, B. H. November, R. G. Povey, S. J. Whiteley, D. D. Awschalom, D. I. Schuster, and A. N. Cleland, Quantum control of surface acoustic-wave phonons, Nature **563**, 661 (2018).

[10] M. Z. Hasan, Colloquium: Topological insulators, Rev. Mod. Phys. **82**, 3045 (2010).

[11] X. Qi and S. Zhang, Topological insulators and superconductors, Rev. Mod. Phys. **83**, 1057 (2011).

[12] B. A. Bernevig, T. L. Hughes, and S. C. Zhang, Quantum spin Hall effect and topological phase transition in HgTe quantum wells, Science **314**, 1757 (2006).

[13] A. B. Khanikaev and G. Shvets, Two-dimensional topological photonics, Nat. Photonics **11**, 763 (2017).

[14] T. Ozawa, H. M. Price, A. Amo, N. Goldman, M. Hafezi, L. Lu, M. C. Rechtsman, D. Schuster, J. Simon, O. Zilberberg, and I. Carusotto, Topological photonics, Rev. Mod. Phys. **91**, 015006 (2019).

[15] L. H. Wu and X. Hu, Scheme for Achieving a Topological Photonic Crystal by Using Dielectric Material, Phys. Rev. Lett. **114**, 223901 (2015).

[16] Z. Wang, Y. Chong, J. D. Joannopoulos, and M. Soljačić, Observation of unidirectional backscattering-immune topological electromagnetic states, Nature **461**, 772 (2009).

[17] A. B. Khanikaev, S. H. Mousavi, W. K. Tse, M. Kargarian, A. H. MacDonald, and G. Shvets, Photonic topological insulators, Nat. Mater. **12**, 233 (2013).

[18] Y. Yang, Y. F. Xu, T. Xu, H. X. Wang, J. H. Jiang, X. Hu, and Z. H. Hang, Visualization of a Unidirectional Electromagnetic Waveguide Using Topological Photonic Crystals Made of Dielectric Materials, Phys. Rev. Lett. **120**, 217401 (2018).

[19] M. I. Shalaev, W. Walasik, A. Tsukernik, Y. Xu, and N. M. Litchinitser, Robust topologically protected transport in photonic crystals at telecommunication wavelengths, Nat. Nanotechnol. **14**, 31 (2019).

[20] X. Cheng, C. Jouvaud, X. Ni, S. H. Mousavi, A. Z. Genack, and A. B. Khanikaev, Robust reconfigurable electromagnetic pathways within a photonic topological insulator, Nat. Mater. **15**, 542 (2016).

[21] S. Peng, N. J. Schilder, X. Ni, J. Van De Groep, M. L. Brongersma, A. Alù, A. B. Khanikaev, H. A. Atwater, and A. Polman, Probing the Band Structure of Topological Silicon Photonic Lattices in the Visible Spectrum, Phys. Rev. Lett. **122**, 117401 (2019).

[22] N. Parappurath, F. Alpeggiani, L. Kuipers, and E. Verhagen, Direct observation of topological edge states in silicon photonic crystals: Spin, dispersion, and chiral routing, Sci. Adv. **6**, eaaw4137 (2020).

[23] S. D. Huber, Topological mechanics, Nat. Phys. **12**, 621 (2016).

[24] J. Paulose, B. G. G. Chen, and V. Vitelli, Topological modes bound to dislocations in mechanical metamaterials, Nat. Phys. **11**, 153 (2015).

[25] L. M. Nash, D. Kleckner, A. Read, V. Vitelli, A. M. Turner, and W. T. M. Irvine, Topological mechanics of gyroscopic metamaterials, Proc. Natl. Acad. Sci. U. S. A. **112**, 14495 (2015).

[26] M. Serra-garcia, V. Peri, R. Süsstrunk, O. R. Bilal, T. Larsen, L. G. Villanueva, and S. D. Huber, Observation of a phononic quadrupole topological insulator, Nature **555**, 342 (2018).

[27] B. G. Chen, B. Liu, A. A. Evans, J. Paulose, I. Cohen, V. Vitelli, and C. D. Santangelo, Topological Mechanics of Origami and Kirigami, Phys. Rev. Lett. **116**, 135501 (2016).

[28] G. Ma, M. Xiao, and C. T. Chan, Topological phases in acoustic and mechanical systems, Nat. Rev. Phys. **1**, 281 (2019).

[29] R. Fleury, D. L. Sounas, C. F. Sieck, M. R. Haberman, and A. Alù, Sound isolation and giant linear nonreciprocity in a compact acoustic circulator, Science **343**, 516 (2014).

[30] J. Lu, C. Qiu, L. Ye, X. Fan, M. Ke, F. Zhang, and Z. Liu, Observation of topological valley transport of sound in sonic crystals, Nat. Phys. **13**, 369 (2017).

[31] C. He, X. Ni, H. Ge, X. Sun, Y. Chen, M. Lu, X. Liu, and Y. Chen, Acoustic topological insulator and robust one-way sound transport, Nat. Phys. **12**, 1124 (2016).

[32] H. He, C. Qiu, L. Ye, X. Cai, X. Fan, M. Ke, F. Zhang, and Z. Liu, Topological negative refraction of surface acoustic waves in a Weyl phononic crystal, Nature **560**, 61 (2018).

[33] W. Tang, X. Jiang, K. Ding, Y. X. Xiao, Z. Q. Zhang, C. T. Chan, and G. Ma, Exceptional nexus with a hybrid topological invariant, Science **370**, 1077 (2020).

[34] M. Weiner, X. Ni, M. Li, A. Alù, and A. B. Khanikaev, Demonstration of a third-order hierarchy of topological states in a three-dimensional acoustic metamaterial, Sci. Adv. **6**, eaay4166 (2020).

[35] X. Ni, M. Weiner, A. Alù, and A. B. Khanikaev, Observation of higher-order topological acoustic states protected by generalized chiral symmetry, Nat. Mater. **18**, 113 (2019).

[36] F. Zangeneh-Nejad and R. Fleury, Topological Fano Resonances, Phys. Rev. Lett. **122**, 14301 (2019).

[37] A. Souslov, K. Dasbiswas, M. Fruchart, S. Vaikuntanathan, and V. Vitelli, Topological Waves in Fluids with Odd Viscosity, Phys. Rev. Lett. **122**, 128001 (2019).

[38] S. H. Mousavi, A. B. Khanikaev, and Z. Wang, Topologically protected elastic waves in phononic metamaterials, Nat. Commun. **6**, 8682 (2015).

[39] S. Y. Yu, C. He, Z. Wang, F. K. Liu, X. C. Sun, Z. Li, H. Z. Lu, M. H. Lu, X. P. Liu, and Y. F. Chen, Elastic

pseudospin transport for integratable topological phononic circuits, Nat. Commun. **9**, 3072 (2018).

[40] M. Miniaci, R. K. Pal, B. Morvan, and M. Ruzzene, Experimental Observation of Topologically Protected Helical Edge Modes in Patterned Elastic Plates, Phys. Rev. X **8**, 31074 (2018).

[41] A. Darabi, X. Ni, M. Leamy, and A. Alù, Reconfigurable Floquet elastodynamic topological insulator based on synthetic angular momentum bias, Sci. Adv. **6**, eaba8656 (2020).

[42] M. Yan, J. Lu, F. Li, W. Deng, X. Huang, J. Ma, and Z. Liu, On-chip valley topological materials for elastic wave manipulation, Nat. Mater. **17**, 993 (2018).

[43] J. Cha, K. W. Kim, and C. Daraio, Experimental realization of on-chip topological nanoelectromechanical metamaterials, Nature **564**, 229 (2018).

[44] H. Ren, T. Shah, H. Pfeifer, V. Peano, F. Marquardt, O. Painter, *Topological phonon transport in an optomechanical system*, arXiv:2009.06174.

[45] T. Wu, L. Wu, and Z. Huang, Frequency bandgap measurement of two-dimensional air/silicon phononic crystals using layered slanted finger interdigital transducers, J. Appl. Phys. **97**, 094916 (2005).

[46] S. Benchabane, A. Khelif, J. Y. Rauch, L. Robert, and V. Laude, Evidence for complete surface wave band gap in a piezoelectric phononic crystal, Phys. Rev. E **73**, 065601 (2006).

[47] A. Khelif, Y. Achaoui, S. Benchabane, V. Laude, and B. Aoubiza, Locally resonant surface acoustic wave band gaps in a two-dimensional phononic crystal of pillars on a surface, Phys. Rev. B **81**, 214303 (2010).

[48] Y. Achaoui, A. Khelif, S. Benchabane, L. Robert, and V. Laude, Experimental observation of locally-resonant and Bragg band gaps for surface guided waves in a phononic crystal of pillars, Phys. Rev. B **83**, 104201 (2011).

[49] S. Benchabane, O. Gaiffe, G. Ulliac, R. Salut, Y. Achaoui, and V. Laude, Guidance of surface waves in a micron-scale phononic crystal line-defect waveguide, Appl. Phys. Lett. **98**, 171908 (2011).

[50] B. J. Ash, S. R. Worsfold, P. Vukusic, and G. R. Nash, A highly attenuating and frequency tailorable annular hole phononic crystal for surface acoustic waves, Nat. Commun. **8**, 174 (2017).

[51] D. Yudistira, A. Boes, B. Djafari-Rouhani, Y. Pennec, L. Y. Yeo, A. Mitchell, and J. R. Friend, Monolithic Phononic Crystals with a Surface Acoustic Band Gap From Surface Phonon-Polariton Coupling, Phys. Rev. Lett. **113**, 215503 (2014).

[52] L. Shao, W. Mao, S. Maity, N. Sinclair, Y. Hu, L. Yang, and M. Lončar, Non-reciprocal transmission of microwave acoustic waves in nonlinear parity–time symmetric resonators, Nat. Electron. **3**, 267 (2020).

[53] S. Y. Yu, X. C. Sun, X. Ni, Q. Wang, X. J. Yan, C. He, X. P. Liu, L. Feng, M. H. Lu, and Y. F. Chen, Surface phononic graphene, Nat. Mater. **15**, 1243 (2016).

[54] See Supplemental Material at http://link.aps.org/supplemental/10.1103/PhysRevApplied.16.044008 for sample preparation, distinction of SAW modes in band-structure calculations, detailed calculation process for the SAW helical edge states, operational bandwidth of the SAW topological insulator, influence of anisotropic substrate, related theory (SAW topological insulator from band inversion), comparison between SAW topological and ordinary waveguides, different bends and defects immune by the SAW topological waveguides, comparison between SAW topological waveguides based on QSHE and QVHE, Video SI (the SAW helical edge states), and Video SII (the Rayleigh-type surface-acoustic-wave modes mainly used in our phononic crystals).

[55] B. Graczykowski, F. Alzina, J. Gomis-Bresco, and C. M. Sotomayor Torres, Finite element analysis of true and pseudo surface acoustic waves in one-dimensional phononic crystals, J. Appl. Phys. **119**, 025308 (2016).

[56] C. Brendel, V. Peano, O. J. Painter, and F. Marquardt, Pseudomagnetic fields for sound at the nanoscale, Proc. Natl. Acad. Sci. U. S. A. **114**, E3390 (2017).

[57] R. E. Christiansen, F. Wang, and O. Sigmund, Topological Insulators by Topology Optimization, Phys. Rev. Lett. **122**, 234502 (2019).

[58] X. Wu, Y. Jin, A. Khelif, X. Zhuang, T. Rabczuk, and B. Djafari-Rouhani, Topological surface wave metamaterials for robust vibration attenuation and energy harvesting, Mech. Adv. Mater. Struct., 1 (2021).

[59] Z. Wang, F. K. Liu, S. Y. Yu, S. L. Yan, M. H. Lu, Y. Jing, and Y. F. Chen, Guiding robust valley-dependent edge states by surface acoustic waves, J. Appl. Phys. **125**, 044502 (2019).

[60] D. Yudistira, A. Boes, D. Janner, V. Pruneri, J. Friend, and A. Mitchell, Polariton-based band gap and generation of surface acoustic waves in acoustic superlattice lithium niobate, J. Appl. Phys. **114**, 054904 (2013).